Combined observation of a dust storm over the Loess Plateau using a dual-wavelength lidar and an aethalometer

Xingai Gao, Xianjie Cao*, Pengfei Tian, Lei Zhang, Zhongwei Huang, Tian Zhou

Key Laboratory for Semi-Arid Climate Change of the Ministry of Education, College of Atmospheric Sciences, Lanzhou University, Lanzhou, China

ABSTRACT

A dust storm was observed at the Semi-Arid Climate and Environment observatory of Lanzhou University (SACOL) using a dual-wavelength lidar and an aethalometer from 16 March to 22 March 2010. After the arrival of the dust storm, the lidar backscattered signal increased suddenly, the volume depolarization ratio ranged from 0.2 to 0.4. The dust aerosol was detected mainly in a layer below 2.5 km altitude. A higher attenuated backscatter coefficient ($0.005-0.02$ km^{-1}/sr) was distributed in a lower layer (below 2.5 km) during the dust storm. The evolution of the dust storm was also clearly revealed by the integrated particle backscatter coefficient (BE). Particles in the coarse mode are predominant during the dust storm because Ångström exponent mainly ranged from 0.5 to 1.0. An aethalometer was used to measure the aerosol absorption coefficient as well as aerosol mass concentration. The average mass concentration of aerosol was 1.3 μg/m^3 during the dust free period but increased to 1.8 μg/m^3 during the dust storm, so the dust aerosol apparently played an important role. The main absorptive particle was black carbon during the dust free period. In addition, the peaks of dust aerosol concentration mainly occurred at around 08:00 and 20:00 (Beijing Time), one reason was that the increase of wind speed result in more dust particles blown up into the atmosphere in the neighborhood of SACOL and another reason was that the boundary layer convection was undeveloped in the morning and the temperature inversion appeared easily in the evening. The trend of the aerosol absorption coefficient was similar to that of mass concentration, and the aerosol absorption coefficient significantly increased during the dust storm.

1. Introduction

Dust aerosol emitted from dry soil surfaces is one of the most influential components of the atmospheric environment in sparsely vegetated areas, deserts and semi-arid areas, and has drawn considerable attention in recent years (Wang et al., 2008; Zhang et al., 2010). Dust aerosol influences the Earth's radiative balance and climate directly and indirectly (Sasano, 1996; Lohmann et al., 2007; Mahowald et al., 2010). On the one hand, it affects the Earth-Atmosphere system energy balance directly through the absorption and scattering of solar radiation (Charlson et al., 1992; Ramanathan et al., 2001; Papayannis et al., 2008; Tian et al., 2017), although the radiative effect of dust aerosol remains uncertain (IPCC, 2013). On the other hand, it changes clouds' optical and physical properties indirectly by forming cloud condensation nuclei and also ice nuclei, and thereby alters the cloud albedo and precipitation (Albrecht, 1989; Twomey, 1991; Rosenfeld et al., 2014). Additionally, dust aerosol can influence ocean and land ecosystems through long-range transport and deposition (Duce et al., 1991; Gao et al., 1997; Herut et al., 2001; Zhang and Gao, 2007).

Many international experiments have been conducted to investigate the radiative properties of dust aerosol, such as the Saharan Dust Experiment (SHADE; Tanré et al., 2003; Highwood et al., 2003) and the Pacific Dust Experiment (PACDEX; Stith et al., 2009). To better understand dust aerosol radiative properties, field experiments have been performed over the arid and semi-arid areas of China in recent years. For instance, the 2008 China-US joint dust field experiment including three sites (Lanzhou, Zhangye, and Jingtai) was conducted over the Loess Plateau, one of the main dust sources in China, to investigate dust aerosol

---

radiative forcing (Li et al., 2007; Huang et al., 2010). In addition, the Japan-China joint project, Aeolian Dust Experiment on Climate Impact (ADEC), was initiated in April 2000 to study the radiative forcing caused by dust aerosol (Mikami et al., 2006).

The vertical distribution of dust aerosol is an important factor in assessing the radiation forcing of dust aerosol (Zhu et al., 2007; Huang et al., 2009). Some researchers have demonstrated that one of the important reasons for the uncertain assessment of dust aerosol radiation forcing was the lacking observations of vertical structure (Nousiainen, 2009; Huang et al., 2010; Zhou et al., 2012). Thus, obtaining the temporal and spatial distribution of dust aerosol is valuable to estimate the radiation forcing of dust aerosol. Remote-sensing techniques such as lidar play an important role in aerosol measurements because of their marked advantages in determining the vertical structure of aerosols (Sasano, 1996; Immler and Schrems, 2003; Zhang et al., 2010; Burton et al., 2015; Tian et al., 2015). Many researchers have used the lidar retrieval algorithm based on the research of Klett-Fernald method (Klett, 1981, 1985; Fernald et al., 1972; Fernald, 1984) to study the vertical structure of aerosols (Welton et al., 2001; Sicard et al., 2009; Pappalardo et al., 2014; Guerrero-Rascado et al., 2016). Here, we introduced the cloud discrimination based on the algorithm of Klett-Fernald method and this improved algorithm was used firstly in analyzing a dust case.

Some measurements have shown that aerosol light absorption plays important roles in radiation forcing (Stier et al., 2007; Moosmüller et al., 2009). Black carbon (BC) is the main absorptive aerosol in urban and biomass-burning environments (Kirchstetter et al., 2004), whereas in and downwind of arid and semi-arid regions, the main absorbing species is dust aerosol (Chin et al., 2009). Many studies have demonstrated that dust aerosol can cause significant absorption at shorter wavelengths (i.e., wavelengths less than 500 nm) (Dickerson et al., 1997; Dubovik et al., 1998). Here, we presented the temporal variation of aerosol concentration and absorption coefficient using aethalometer during a dust storm.

Observations for the present study were conducted at the Semi-Arid Climate and Environment Observatory of Lanzhou University (SACOL, 35°57′N, 104°08′E, 1965.8 m) during a dust storm that occurred from 16 March 2010 to 22 March 2010. In this paper, a dual-wavelength lidar was employed to analyze the temporal variation of the 532 nm backscattered signal, volume depolarization ratio, particle backscatter coefficient, backscatter-related Ångström exponent and integrated particle backscatter coefficient. An aethalometer was employed to analyze aerosol mass concentration and absorption coefficient.

2. Site description and instrumentation

SACOL is located on the hilltop in Cuiying approximately 48 km away from the center of Lanzhou on the Loess Plateau of China (Huang et al., 2008). The topography around the site is characterized by the Loess Plateau, which contains plains, ridges and mounds with an elevation ranging from 1714 to 2089 m. The site is primarily covered by stipabungeana, artemisia frigid and leymussecalinus. The more detailed information can be found in the literature by Huang et al. (2008). The instruments used in this study included a dual-wavelength lidar and an aethalometer.

The dual-wavelength (1064 nm, 532 nm) lidar (L2S-SM II, NIES, Japan) employs a flash-lamp-pumped Nd:YAG laser as a second harmonics generator and a 20-cm Schmidt Cassegrain telescope as a receiver. The received signal is collimated and separated to the 532 and 1064 nm channels, and the 532 nm signal is separated into two independent polarization channels in parallel and

perpendicular directions to conduct the polarization detection (Cao et al., 2014). The lidar observation reported here was made with a time interval of 15 min and a range resolution of 6 m.

The seven-wavelength aethalometer (AE-31, Magee scientific Inc., USA) can monitor the concentration of black carbon (BC) and elemental carbon (EC) in the atmosphere. The aethalometer uses an optical source assembly that incorporates seven different solid-state light sources: 370, 470, 520, 590, 660, 880 and 950 nm. The amount of BC accumulated on the fibrous quartz filter is linearly proportional to the attenuation of a beam of light transmitted through the aerosol sample. The algorithm introduces a variable $ATN(\lambda)$ to represent filter attenuation through the sample spot as: $ATN(\lambda) = 100 \cdot ln(I_1/I_2)$, where I_1 and I_2 are respectively transmission light intensities of the reference and the sample beams at time t_1 and t_2 (sec).

Black carbon concentration can be calculated using the following equation:

$$MBC = \frac{A \cdot ATN(\lambda)}{\sigma \cdot Q(t_2 - t_1)}, \tag{1}$$

where MBC is the mass concentration of BC, A (m^2) is the area of a filter spot, σ (m^2/g) is the attenuation cross-section of BC, Q (L/min) is the sampling flow. For BC observation, $\sigma = 14625/\lambda$. The values of σ come from the literature of Hansen (2005). The absorption coefficient can be obtained by the equation of $BC_{abs} = MBC \cdot \sigma$. Table 1 presents the values of σ in different bands. In consideration of the lidar wavelength of 532 nm, in this paper we mainly analyzed the aerosol mass concentration and absorption coefficient at 520 nm.

3. Lidar data corrections

The corrections of lidar data are essential to get high quality results. The correction of NIES mainly included the range square correction, overlap correction and background noise subtraction. In this paper, geometrical overlap factor is determined by the method of Huang (2012). Firstly, we calculated the geometrical overlap factor of MPL lidar by Slope Method (Dho et al., 1997) through horizontal observation at SACOL. Then we selected the same observation period of NIES lidar (near to MPL) as MPL and calculated the constant ratio between the signal intensity of MPL to the signal intensity of NIES above a certain distance (geometrical overlap factor is 1). Finally, the geometrical overlap factor of NIES can be calculated by an equation about the constant ratio and the geometrical overlap factor of MPL. Fig. 1 shows the lidar geometric factor of NIES. More description about this method can be seen in the literature of Huang (2012).

The depolarization ratio has been calibrated about s and p channels before using the data. The calibration method was adapted from the research of Freudenthalter et al. (2009), which rotated the polarizing beam splitter (PBS) to 90° from original position to obtain a new measured depolarization ratio, and then compared the new measured depolarization ratio with the original

Table 1
The optical sources of aethalometer.

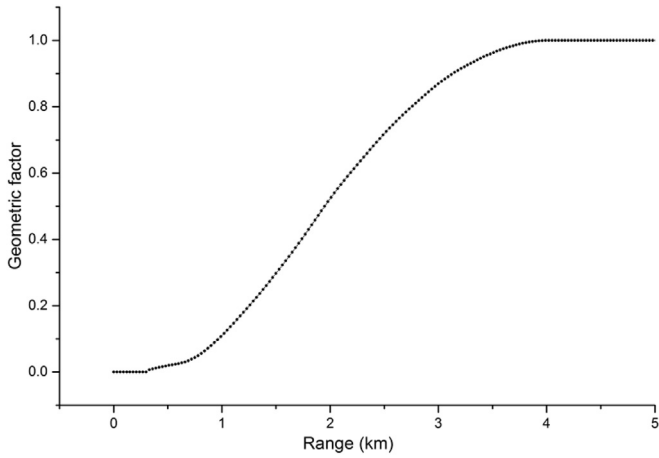| Channel	Wavelength (nm)	σ (BC) (m^2/g)
UV	370	39.5
Blue	470	31.1
Green	520	28.1
Yellow	590	24.8
Red	660	22.2
IR-1	880	16.6
IR-2	950	15.4

Fig. 1. The distribution of lidar geometric factor.

measured depolarization ratio getting the correction factor. More description about this method can be seen in the literature of Freudenthalter et al. (2009).

4. Cloud discrimination of the lidar data

The cloud discrimination approach used in this paper was adapted from the methods of Mao et al. (2011) and Cao et al. (2014). In general, the signal value increases to the peak firstly and then decreases rapidly when the lidar backscattered signal encounters a cloud in the atmosphere. In the range between the cloud base to cloud peak (base to peak range, BPR), the signal is smaller than that of the central range bin in the first half of the window and the signal is greater than the central range bin in the other half of the window, as shown in Fig. 2. So we determine the cloud base height and the cloud peak height by defining a trend function $f(R) = a + b - 0.5c$, where a is the number of range bins whose range-corrected signal (RCS) is weaker than that of the central range bin in the first half of the window, b is the number of range bins whose RCS is greater than that of the central range bin in the other half of the window and c is the number of range bins in the window. The positive value of $f(R)$ denotes that the backscattered signal increases with height.
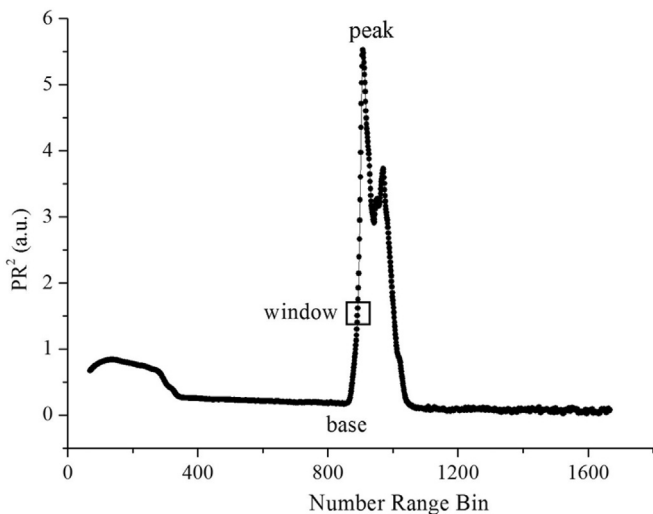

Fig. 2. A lidar signal includes a cloud layer and the peak and base of cloud have been marked out. The rectangle represents the window we calculate.

In this paper, we select $f(R) = 0$ as the threshold value. If the value of $f(R)$ is positive, the window is enlarged and we will continue to calculate $f(R)$ until it equals to zero. The selected window can be seen a candidate for BPR. The range bin where the maximum of the RCS appears is considered to be the peak, and the initial range bin is the base. If $RCS_{peak}/RCS_{base} > 2$, the selected window is considered to be the cloud layer. We need to reject over-detection caused by noise variations based on the original signal by using $\Delta = P(R_{Peak}) - P(R_{base}) < \sigma$, where $P(R)$ is the lidar original signal at range R and σ is the standard deviation of $P(R)$ in the range of 15−17 km, which is close to that of clear air. Finally, the cloud base height must be adjusted to prevent its underestimation. If $\sigma_1 < 2\sigma$, the cloud base height would be reset at the height of a range bin above the former cloud base height, where σ_1 is the standard deviation of $P(R)$ in the range between the cloud base height and nine range bins above the cloud base height.

5. Retrieval algorithm

The algorithm in this paper was designed based on the inversion methods of Fernald et al. (1972), Fernald (1984) and Klett (1981, 1985). This algorithm was designed to obtain the aerosol backscatter coefficient. The lidar equation can be written as:

$$P(z) = ECz^{-2}[\beta_1(z) + \beta_2(z)]T_1^2(z)T_2^2(z), \tag{2}$$

where z is the range from the particle to the lidar, $P(z)$ is the corrected lidar backscattered signal, E is the transmitted laser pulse energy, C is the system calibration constant, $\beta(z)$ is the atmospheric backscatter coefficient, $T(z) = exp[-\int_0^z \alpha(z)dz]$ is the transmittance and $\alpha(z)$ is the extinction coefficient. The subscripts 1 and 2 stand for aerosol and atmospheric molecules, respectively. Then, by introducing the lidar ratio S (Cao et al., 2013), the solution to Equation (2) for aerosol backscatter coefficient can be written as follows:

$$\beta_1(z) = \frac{P(z)z^2 exp\left[-2(S_1 - S_2)\int_0^z \beta_2(z)dz\right]}{CE - 2S_1\int_0^z P(z)z^2 exp\left[-2(S_1 - S_2)\int_0^z \beta_2(\dot{z})d\dot{z}\right]dz} - \beta_2(z), \tag{3}$$

where S_2 has a constant value of $8\pi/3$, β_2 can be obtained via Rayleigh scattering theory using the US standard atmospheric profile and initialized with the temperature and pressure values measured at the lidar site (Balin et al., 2004), S_1 is the aerosol extinction-to-backscatter ratio. If the aerosol extinction coefficient at the reference height z_c is available, then Equation (3) leads to a numerical integration. To stabilize the solution, we select the backward solution in this paper (Klett, 1981; Zhang et al., 2010). Then, the 532 nm integrated particle backscatter coefficient (BE) can be obtained by integrating the backscatter coefficient from ground to z_c.

In the retrieval, three parameters must first be obtained including the reference height z_c, the aerosol extinction coefficient at z_c and the aerosol extinction-to-backscatter ratio (S_1). In this paper, the reference height is set at the cloud base height if a cloud is present in the atmosphere. Otherwise, it is set at a height with negligible particle loading, where contribution to the extinction coefficient arises only from air molecules (Balis et al., 2006; Cao

et al., 2013). Additionally, we set S_1 to 45 sr at 532 nm and 33 sr at 1064 nm obtained from the study of Wang et al. (2012), who analyzed six dust events using the modified Sasano-Browell method from March to April 2010 at SACOL.

In this paper, we can also obtain the backscatter-related Ångström exponent (532/1064), the definition of which can be written as

$$AE_\beta = \frac{-\ln(\beta_{\lambda_1}/\beta_{\lambda_2})}{\ln(\lambda_1/\lambda_2)}, \qquad (4)$$

where λ_1 and λ_2 represent two reference wavelengths (532 nm and 1064 nm), β_{λ_1} and β_{λ_2} are the aerosol backscatter coefficient at 532 nm and 1064 nm respectively, and AE_β is the Angstrom exponent. This parameter is known to be dependent on particle size and shape. The value of Ångström exponent (AE_β) is 4 for molecules and varies between 0 and 2 for particles (Russell et al., 2009) with smaller Ångström exponents corresponding to larger particles and vice-versa.

6. Results and discussion

This dust storm arrived over SACOL at 17:00 (Beijing Time, 1 h and 3 min earlier than Lanzhou local time) on 16 March 2010. Fig. 3 presents the distribution of the 500 hPa geopotential height and potential temperature in Eurasia using NCEP/NCAR reanalysis data (2.5° × 2.5°) at 20:00 on 16 March. From the Caspian Sea and the Aral Sea to the north of Xinjiang, China, extended a high hot ridge, which influenced the easterly movement of the weather system. In addition, a transverse slot from northeastern China to southern Mongolia affected the future weather conditions in China by shifting to a vertical orientation. SACOL was located at the front of the high hot ridge and downstream of the transverse slot.

Fig. 4a shows an MODIS image taken on 16 March 2010, illustrating the overpass of a dust storm across the Loess Plateau. In order to describe this dust event over Loess Plateau, the HYSPLIT.4 model (Draxler and Rolph, 2003) has been used to calculate five-day backtrajectories of air masses at three different altitudes above ground level (a.g.l.) using the GDAS database (Global Data Assimilation System, ftp://www.arl.noaa.gov/pub/archives/gdas1/), as Fig. 4b shows. From the backward trajectory distribution, the northwest wind was dominant during the period of this dust storm and the main source of dust particles was the Taklimakan Desert (2000m a.g.l.) and the desert closed to Dunhuang (500 and 1500 m a.g.l.).

Fig. 5 shows the wind rose during a time period from 16 March to 22 March 2010, for which data on wind direction and speed at 2 m above the ground every 3 h were obtained from the Yuzhong station, 7 km from SACOL. A northerly wind was dominant over SACOL, and the fraction of mostly northerly wind was more than 10%, the northwesterly wind reaching a maximum of 7 m/s. In addition, the southwesterly wind was the second major wind direction and its frequency was also more than 10%.

Fig. 6 displays (a) the temporal evolution of the surface temperature, (b) relative humidity, (c) wind speed, (d) integrated particle backscatter coefficient (BE) and (e) backscatter-related Ångström exponent. Data regarding surface temperature and relative humidity (HMP45C-L, Vaisalla), wind speed (014A-L, Met One) at 2 m were obtained to analyze the basic meteorological conditions, integrated particle backscatter coefficient (BE) and Ångström exponent were retrieved by lidar. The variation trends of surface temperature and relative humidity were opposite to each other. For example, the highest temperature was at approximately 17:00 and the lowest temperature was at approximately 04:00 every day, while the distribution of relative humidity was the opposite. The highest surface temperature was 23.8 °C during the dust free period, but the highest temperature was less than 20 °C during the dust storm, especially dropping below 11 °C at 17:00, 20 March (Fig. 6a). Thus, the dust aerosol may have a cooling effect on the ground. Before the arrival of the dust storm, the surface relative humidity rapidly decreased from 60% at 08:00 to 14% at 17:00, 16 March. In addition, the relative humidity was maintained at a low level from 16:00, 17 March, to 16:00, 19 March, and the maximum was less than 35% (Fig. 6b). Thus, the atmosphere was in a relative dry state before the arrival of the dust storm. In short, before the arrival of the dust storm, the atmosphere was in a dry, high-temperature state, which promoted instability and enhanced convection beneficial to the occurrence of the dust storm. The distribution of the BE had four peaks, and these four peaks corresponded to sudden increases in wind speed (Fig. 6c and d) (the gap in Fig. 6d is no signal region where NIES Lidar had no signal). A sudden increase in wind speed contributed to the process of floating dust. The BE was less than 0.01 before the arrival of the dust storm (08:00 to 17:00, 16 March) but increased rapidly to 0.015 after the dust storm arrived. Most of the BE values ranged from 0.01 to 0.03 during the dust storm, which was obviously related to the dust aerosol. The average value of the BE was 0.012 during the dust storm, which was higher than it was during the dust free period (less than 0.005) (Fig. 6d). The distribution of Ångström exponent is
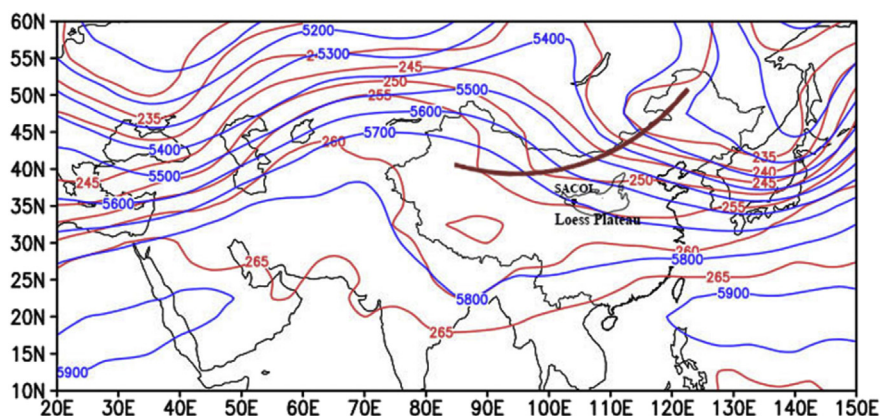

Fig. 3. Distributions of 500 hPa geopotential height (blue line) and potential temperature (red line) at 20:00, 16 March 2010. A brown solid line represents a transverse slot.
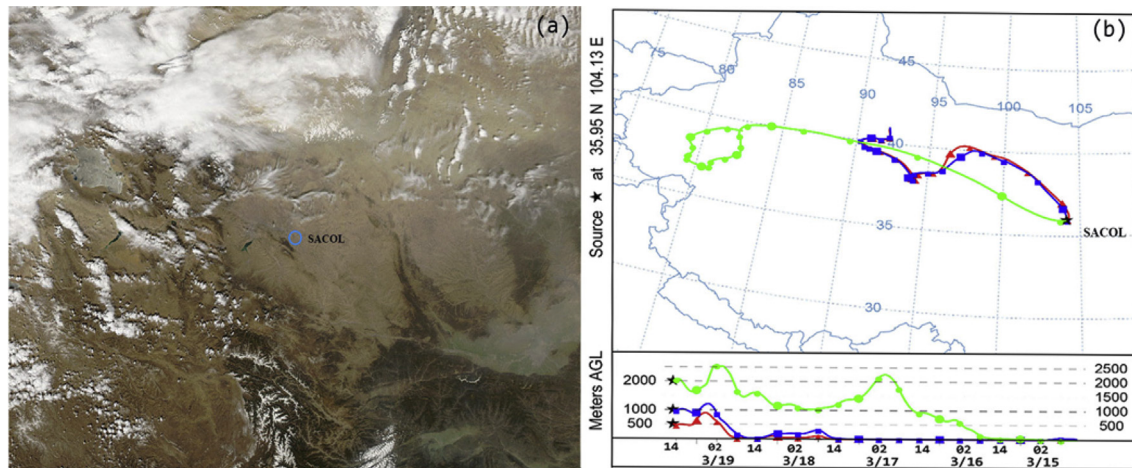
Fig. 4. (a) MODIS true color image observed by the MODIS Aqua on 16 March 2010, (b) Result of the HYSPLIT model 5-day backward trajectory analysis started at altitudes of 500, 1000 and 2000 m at 15:00 Beijing Time at SACOL station on 19 March 2010. The top and bottom panels display horizontal and vertical motion.

roughly inverse to that of BE. The four peaks of BE corresponded to four valleys of Ångström exponent, respectively. The value of Ångström exponent mainly ranged from 1.0 to 2.0, implying the dominance of fine mode particles during the dust free period. The value of Ångström exponent mainly ranged from 0.5 to 1.0 during the dust storm, implying the large fraction of coarse mode particles (Fig. 6e).

Fig. 7 shows (a) the temporal evolution of the 532 nm back-scattered signal, (b) the 532 nm volume depolarization ratio for lidar from 16 March to 22 March 2010 (the gap in Fig. 6 is no signal regions where NIES lidar had no signal). According to the Sand-Dust Weather Almanac (2010), this dust storm can be divided into the following two sub-process: first one is the process of floating dust from 16 March to 17 March, and second one is the process of blowing dust from 19 March to 22 March. Fig. 6 shows that this dust storm began at 17:00, 16 March, and the backscattered signal was weak before 17:00, 16 March. After the dust storm arrived, the backscattered signal increased in the lower layer and the dust aerosol was mainly distributed in the region approximately 2.5 km a.g.l. (Fig. 7a). Furthermore, the volume depolarization ratio changed obviously after the dust storm arrived. The volume

depolarization ratio, an indicator of the presence of non-spherical particles or ice crystals, ranged from 0.2 to 0.4 after the dust storm arrived because dust particles are typically non-spherical (Hu et al., 2007). In contrast, the volume depolarization ratio ranged from 0.1 to 0.2 during the dust free period (Fig. 7b). Zhou et al. (2012) noted that the mean value of the depolarization ratio was 0.3 over SACOL during the dust storm. Huang et al. (2010) also pointed out the dust aerosol had high depolarization ratio (larger than 0.3) over Northwest China. Freudenthalter et al. (2009) found the depolarization ratio of Sahara dust aerosol over the Morocco station was 0.31.

Fig. 8 shows the temporal evolution of the attenuated back-scatter coefficient at 532 nm. We can see that there was a sudden increase in attenuated backscatter coefficient at 17:00, 16 March. A higher attenuated backscatter coefficient (0.005−0.02 km^{-1}/sr) was distributed in the lower layer (below 2.5 km) during the dust storm and was distinct from the attenuated backscatter coefficient during the dust free period (<0.005 km^{-1}/sr).

Fig. 9 shows the vertical distribution of the attenuated back-scatter coefficient in three different cases. Firstly, dust aerosol was mainly observed in the layer below 2.5 km, which was similar to the result shown in Fig. 7. Secondly, the aerosol attenuated backscatter coefficient magnitude was rather small during the dust free period (close to 0 km^{-1}/sr), while the attenuated backscatter coefficient during the dust storm was significantly larger than that of the dust free period, in some cases even closed to 0.02 km^{-1}/sr.

Fig. 10 (a) shows the temporal evolution of the aerosol mass concentration. Three peaks occurred in the distribution of aerosol mass concentration. The distribution periods of the three peaks were similar to those of first three peaks of the integrated particle backscatter coefficient, but the last peak disappeared in Fig. 10, mainly due to observation principle differences in instruments. The lidar is the instrument using remote sensing observation, but the aethalometer is the instrument that measures aerosol mass concentration deposited in the quartz filter. The dust aerosol distributed in the altitude of 2 km and there were no dust particles near the ground from 08:00 to 23:00, 22 March (Fig. 7a), so the deposition of aerosol on the filter was very small (Fig. 10a). The highest aerosol mass concentration was 3.0 μg/m^3 during the dust free period, but the highest value was 5.5 μg/m^3 during the dust storm. In addition, the average aerosol mass concentration was 1.3 μg/m^3 during the dust free period but increased to 1.8 μg/m^3 during the
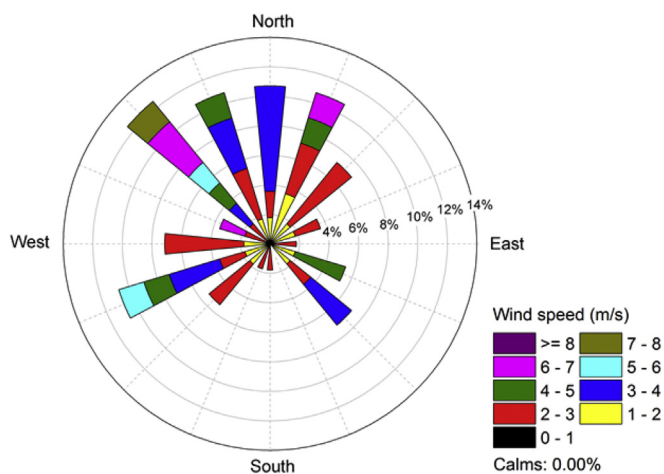

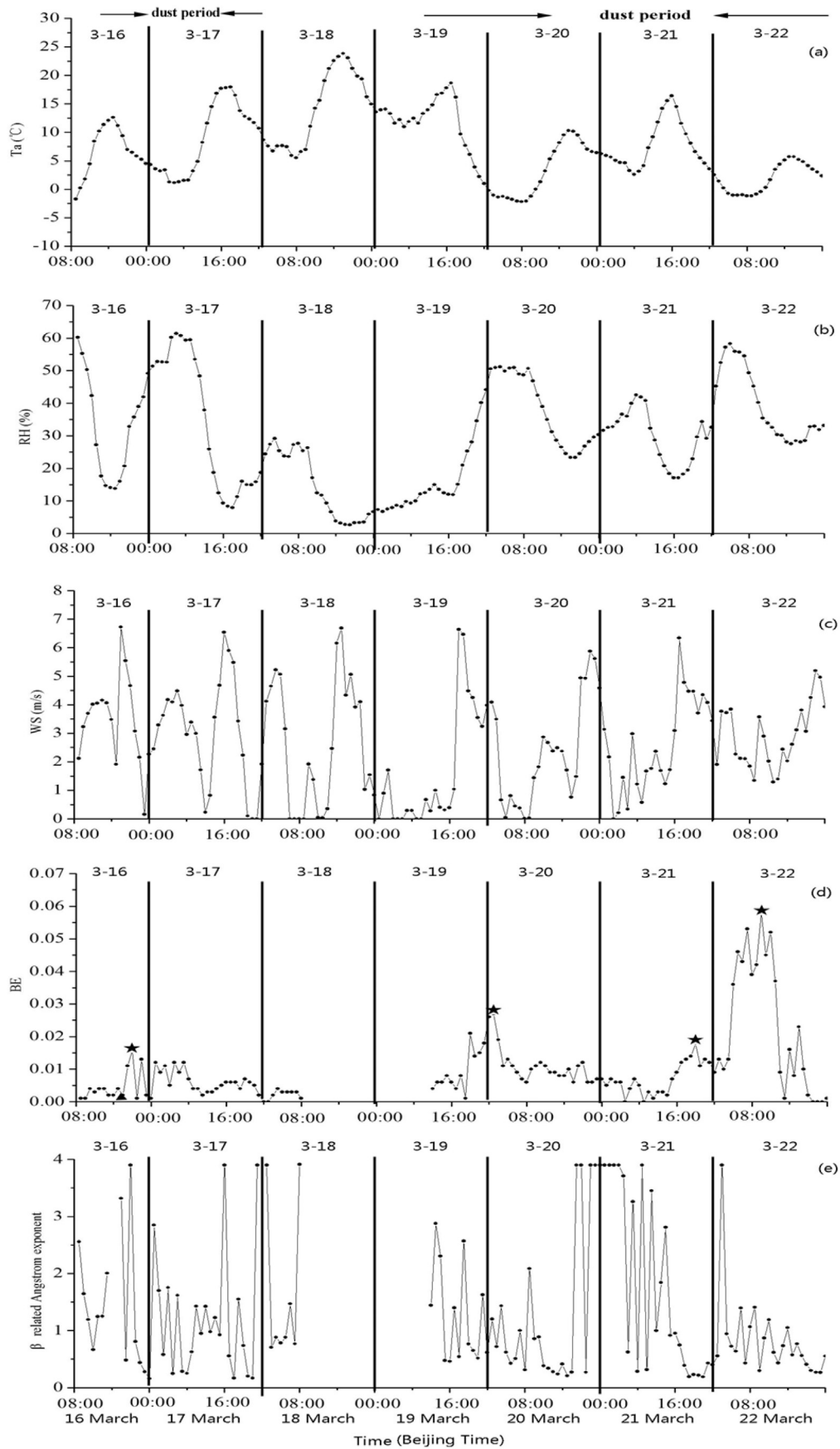**Fig. 5.** Wind rose for the period 16 March to 22 March 2010.

Fig. 6. Temporal evolutions of (a) surface temperature, (b) surface relative humidity, (c) wind speed, (d) the integrated particle backscatter coefficient (BE) and (e) backscatter-related Ångström exponent (532/1064) from 08:00, 16 March, to 23:00, 22 March 2010. The five-pointed stars represent peaks of BE and the triangle represents the time that dust storm arrived.
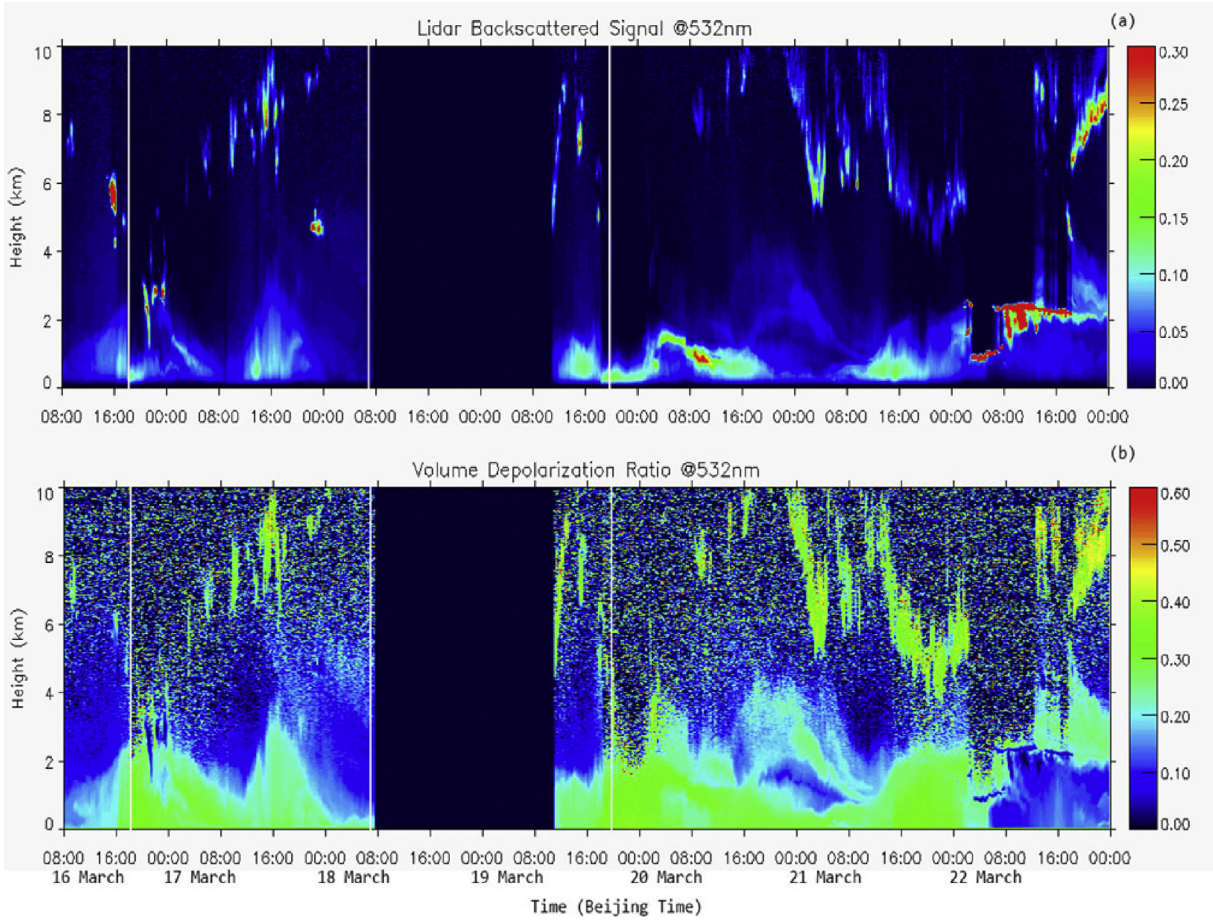
Fig. 7. Vertical structures from lidar measurement: (a) 532 nm backscattered signal, (b) 532 nm volume depolarization ratio. The three solid lines of each panel correspond to the three moments of Fig. 9.

dust storm; hence, the dust aerosol apparently played an important role. The main absorptive particle was black carbon during the dust free period. Zhang et al. (2011) studied the concentration of black carbon using the AE-31 at 880 nm in the station of SACOL, they found that the average concentration of black carbon in SACOL was 1.2 μg/m^3 in spring and the average concentration of black carbon was 2.0 μg/m^3 during the period of dust storm from 27 March 2010

to 29 March 2007. In addition, the aerosol mass concentration peaked at around 08:00 and 20:00 each day, the main reasons included two points: (1) the three peaks of the aerosol mass concentration are accompanied with three dramatic increases in wind speed, the increases of wind speed resulted in more dust particles blown up into the atmosphere in the neighborhood of SACOL; (2) the boundary layer convection was undeveloped in the morning,
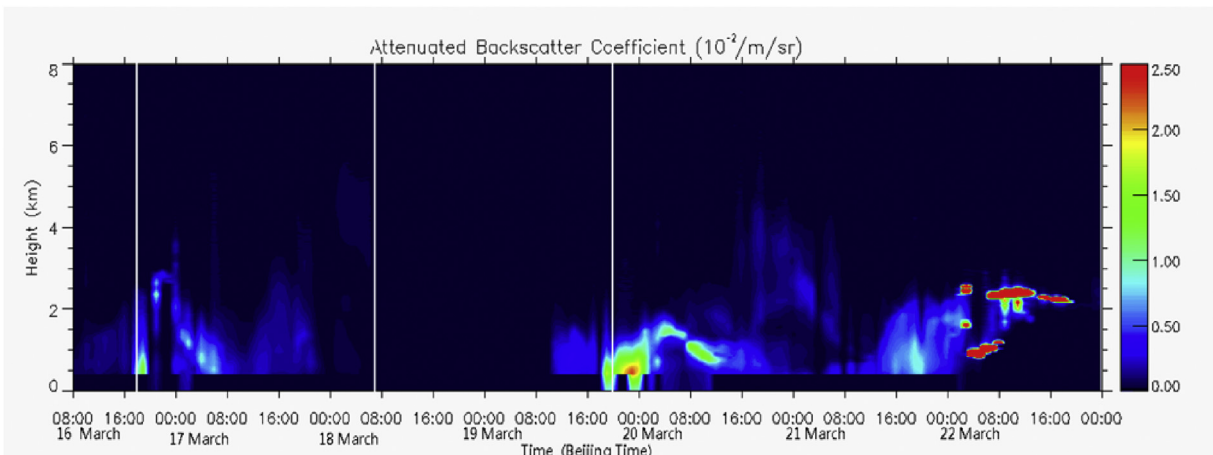

Fig. 8. Temporal evolution of 532 nm attenuated backscatter coefficient in a vertical section from lidar. The three solid lines correspond to the three moments of Fig. 9.
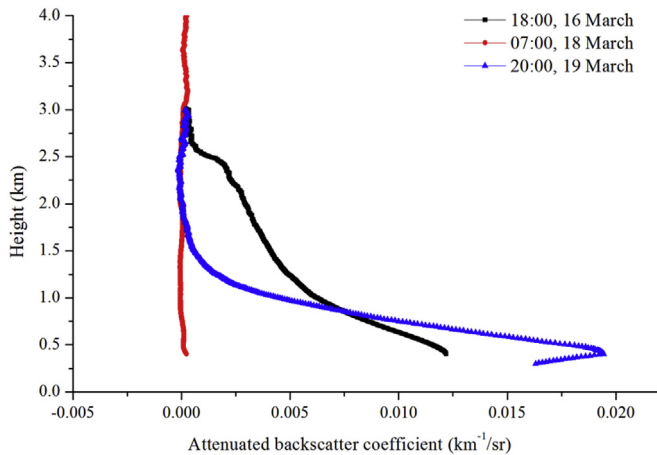
Fig. 9. Vertical profiles of the dust aerosol attenuated backscatter coefficient. The blue and black profiles were obtained under dust storm conditions, and the red profile was obtained under dust free condition.

which had an unfavorable influence on pollutant dispersion. In addition, reduced intensity of solar radiation reaching the ground in the evening, which promoted the formation of a temperature inversion with gathering dust particles on the ground, creating a peak in the evening. Fig. 10 (b) shows the temporal evolution of the aerosol absorption coefficient. The trend of the aerosol absorption coefficient was similar to that of the mass concentration. The main absorptive particle was black carbon in the atmosphere during the dust free period, and the average value of the absorption coefficient was 0.03 km^{-1}, the highest value of the absorption coefficient was

0.08 km^{-1}. After the dust storm arrived, the average value of the absorption coefficient increased to 0.05 km^{-1}, and the highest value was 0.15 km^{-1}. This change was obviously related to the role of dust particles because of their capacity in absorbing visible light (Gillespie and Lindberg, 1992).

7. Summary

In this study, a dust storm process was analyzed during the period from 16 March to 22 March 2010 by using the data of ground-based instruments at the Semi-Arid Climate and Environment Observatory of Lanzhou University (SACOL) on the Loess Plateau of northwestern China. We studied the optical and radiative properties of the dust aerosol, such as attenuated backscatter coefficient, volume depolarization ratio and absorption coefficient. The main results drawn from this paper are summarized as follows:

The aerosol backscattered signal increased in the lower layer when the dust storm arrived. The volume depolarization ratio ranged from 0.2 to 0.4 during the dust storm. The Ångström exponent mainly ranged from 0.5 to 1.0 during the dust storm implying that the coarse mode particles were predominant in dust storm period. The attenuated backscatter coefficient was distributed from 0.005 to 0.02 (km^{-1}/sr) in the lower layer (below 2.5 km) during the dust storm. The average value of the integrated particle backscatter coefficient was 0.012 during the dust storm.

In addition, the aerosol mass concentration and the absorption coefficient were obtained by aethalometer. The average aerosol mass concentration was 1.8 μg/m^3 during the dust storm, and the highest value was 5.5 μg/m^3. Furthermore, the average value of the aerosol absorption coefficient during the dust storm was 0.05 km^{-1}, and the highest value was 0.15 km^{-1}.
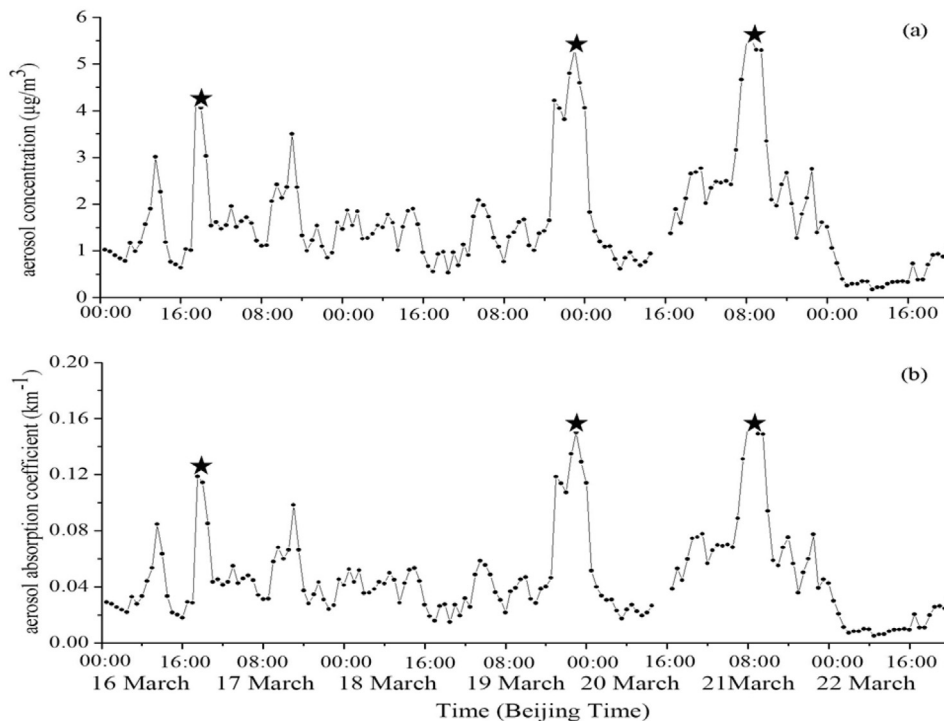

Fig. 10. Temporal evolution at 520 nm of (a) aerosol concentration from 08:00, 16 March, to 23:00, 22 March 2010, (b) aerosol absorption coefficient from 08:00, 16 March, to 23:00, 22 March 2010. The peak of aerosol concentration and absorption coefficient was marked with five-pointed star.

Acknowledgments

References

Albrecht, B.A., 1989. Aerosols, cloud microphysics, and fractional cloudiness. Sci. (New York, N.Y.) 245 (4923), 1227–1230.

Balin, I., Serikov, I., Bobrovnikov, S., Simeonov, V., Calpini, B., Arshinov, Y., van den Bergh, H., 2004. Simultaneous measurement of atmospheric temperature, humidity, and aerosol extinction and backscatter coefficients by a combined vibrational? pure-rotational Raman lidar. Appl. Phys. B 79 (6), 775–782.

Balis, D., Amiridis, V., Kazadzis, S., Papayannis, A., Tsaknakis, G., Tzortzakis, S., Kalivitis, N., Vrekoussis, M., Kanakidou, M., Mihalopoulos, N., Chourdakis, G., Nickovic, S., Pérez, C., Baldasano, J., Drakakis, M., 2006. Optical characteristics of desert dust over the East Mediterranean during summer: a case study. Ann. Geophys. 24 (3), 807–821.

Burton, S.P., Hair, J.W., Kahnert, M., Ferrare, R.A., Hostetler, C.A., Cook, A.L., Harper, D.B., Berkoff, T.A., Seaman, S.T., Collins, J.E., Fenn, M.A., Rogers, R.R., 2015. Observations of the spectral dependence of linear particle depolarization ratio of aerosols using NASA langley airborne high spectral resolution lidar. Atmos. Chem. Phys. 15 (23), 13453–13473.

Cao, X., Wang, Z., Tian, P., Wang, J., Zhang, L., Quan, X., 2013. Statistics of aerosol extinction coefficient profiles and optical depth using lidar measurement over Lanzhou, China since 2005–2008. J. Quant. Spectrosc. Radiat. Transf. 122, 150–154.

Cao, Xianjie, Liang, Jiening, Tian, Pengfei, Zhang, Lei, Quan, Xiaojing, Liu, Weiping, 2014. The mass concentration and optical properties of black carbon aerosols over a semi–arid region in the northwest of China. Atmos. Pollut. Res. 5 (4), 601–609.

Charlson, R.J., Schwartz, S.E., Hales, J.M., Cess, R.D., Coakley Jr., J.A., Hansen, J.E., Hofmann, D.J., 1992. Climate forcing by anthropogenic aerosols. Sci. (New York, N.Y.) 255 (5043), 423–430.

Chin, M., Diehl, T., Dubovik, O., Eck, T.F., Holben, B.N., Sinyuk, A., Streets, D.G., 2009. Light absorption by pollution, dust, and biomass burning aerosols: a global model study and evaluation with AERONET measurements. Ann. Geophys. 27, 3439–3464.

Dho, Sang Whoe, Park, Young Je, Kong, Hong Jin, 1997. Application of geometrical form factor in differential absorption lidar measurement. Opt. Rev. 4 (4), 521–526.

Dickerson, R.R., Kondragunta, S., Stenchikov, G., Civerolo, K.L., Doddridge, B.G., Holben, B.N., 1997. The impact of aerosols on solar ultraviolet radiation and photochemical smog. Sci. (New York, N.Y.) 278 (5339), 827–830.

Draxler, R.R., Rolph, G.D., 2003. NOAA Air Resources Laboratory. availabla at, Silver Spring, MD. http://www.arl.noaa.gov/ready/hysplit4.html.

Dubovik, O., Holben, B.N., Kaufman, Y.J., Yamasoe, M., Smirnov, A., Tanré, D., Slutsker, I., 1998. Single-scattering albedo of smoke retrieved from the sky radiance and solar transmittance measured from ground. J. Geophys. Res. Atmos. 103 (D24), 31903–31923.

Duce, R.A., Liss, P.S., Merrill, J.T., Atlas, E.L., Buat-Menard, P., Hicks, B.B., Miller, J.M., Prospero, J.M., Arimoto, R., Church, T.M., Ellis, W., Galloway, J.N., Hansen, L., Jickells, T.D., Knap, A.H., Reinhardt, K.H., Schneider, B., Soudine, A., Tokos, J.J., Tsunogai, S., Wollast, R., Zhou, M., 1991. The atmospheric input of trace species to the world ocean. Glob. Biogeochem. Cycles 5 (3), 193–259.

Fernald, Frederick G., Herman, Benjamin M., Reagan, John A., 1972. Determination of aerosol height distributions by lidar. J. Appl. Meteorol. 11 (3), 482–489.

Fernald, F.G., 1984. Analysis of atmospheric lidar observations: some comments. Appl. Opt. 23, 652–653.

Freudenthalter, V., Esselborn, M., Wiegner, M., Heese, B., Tesche, M., Ansmann, A., Müller, D., Althausen, D., Wirth, M., Fix, A., Ehret, G., Knippertz, P., Toledano, C., Gasteiger, J., Gerhammer, M., Seefeldner, C., 2009. Depolarization ratio profiling at several wavelengths in pure Saharan dust during SAMUM 2006. Tellus B 61, 165–179.

Gao, Y., Arimoto, R., Duce, R.A., Zhang, X.Y., Zhang, G.Y., An, Z.S., Chen, L.Q., Zhou, M.Y., Gu, D.Y., 1997. Temporal and spatial distributions of dust and its deposition to the China Sea. Tellus B Chem. Phys. Meteorol. 49 (2), 172–189.

Gillespie, J.B., Lindberg, J.D., 1992. Ultraviolet and visible imaginary refractive index of strongly absorbing atmospheric particulate matter. Appl. Opt. 31, 2112–2115.

Guerrero-Rascado, J.L., Landulfo, E., Antuña, J.C., Barbosa, H.M.J., Barja, B., Bastidas, A.E., Bedoya, A.E., da Costa, R.F., Estevan, R., Forno, R.N., Gouveia, D.A.,

Jimenez, C., Larroza, E.G., Lopes, F.J.S., Montilla-Rosero, E., Moreira, G.A., Nakaema, W.M., Nisperuza, D., Alegria, D., Múnera, M., Otero, L., Papandrea, S., Pawelko, E., Quel, E.J., Ristori, P., Rodrigues, P.F., Salvador, J., Sánchez, M.F., Silva, A., 2016. Latin American Lidar Network (LALINET) for aerosol research: diagnosis on network instrumentation. J. Atmos. Sol. Terr. Phys. 138–139, 112–120.

Hansen, A.D.A., 2005. The Aethalometer, Manual. Magee Scientific, Berkeley, California, USA.

Herut, Barak, Nimmo, Malcolm, Medway, Angela, Chester, Roy, Krom, Michael D., 2001. Dry atmospheric inputs of trace metals at the Mediterranean coast of Israel (SE Mediterranean): sources and fluxes. Atmos. Environ. 35 (4), 803–813.

Highwood, E.J., Haywood, J.M., Silverstone, M.D., Newman, S.M., Taylor, J.P., 2003. Radiative properties and direct effect of Saharan dust measured by the C-130 aircraft during Saharan Dust Experiment (SHADE): 2. Terrestrial spectrum. J. Geophys. Res. 108 (D18).

Hu, Y., Vaughan, M., Liu, Z., Lin, B., Yang, P., Flittner, D., Hunt, B., Kuehn, R., Huang, J., Wu, D., Rodier, S., Powell, K., Trepte, C., Winker, D., 2007. The depolarization-attenuated backscatter relation: CALIPSO lidar measurements vs. theory. Opt. Express 15, 5327–5332.

Huang, Jianping, Zhang, Wu, Zuo, Jinqing, Bi, Jianrong, Shi, Jinsen, Wang, Xin, Chang, Zhoulin, Huang, Zhongwei, Yang, Su, Zhang, Beidou, Wang, Guoyin, Feng, Guanghong, Yuan, Jiuyi, Zhang, Lei, Zuo, Hongchao, Wang, Shigong, Fu, Congbin, Jifan, Chou, 2008. An overview of the semi-arid climate and environment research observatory over the loess plateau. Adv. Atmos. Sci. 25 (6), 906–921.

Huang, J., Fu, Q., Su, J., Tang, Q., Minnis, P., Hu, Y., Yi, Y., Zhao, Q., 2009. Taklimakan dust aerosol radiative heating derived from CALIPSO observations using the Fu-Liou radiation model with CERES constraints. Atmos. Chem. Phys. 9, 4011–4021.

Huang, Zhongwei, Huang, Jianping, Bi, Jianrong, Wang, Guoyin, Wang, Wencai, Fu, Qiang, Li, Zhanqing, Tsay, Si-Chee, Shi, Jinsen, 2010. Dust aerosol vertical structure measurements using three MPL lidars during 2008 China-U.S. joint dust field experiment. J. Geophys. Res. 115.

Huang, Z., 2012. Study of Physical and Optical Properties of Atmospheric Aerosols Using Lidar. Ph.D. Thesis. Lanzhou University, china (chinese).

Immler, F., Schrems, O., 2003. Vertical profiles, optical and microphysical properties of Saharan dust layers determined by a ship-borne lidar. Atmos. Chem. Phys. 3, 1353–1364.

IPCC (Intergovernmental Panel on Climate Change), 2013. Climate Change 2013: the Physical Science Basis, the Working Group I Contribution to the UN IPCC's Fifth Assessment Report (WG1 AR5), pp. 159–254. New York.

Klett, J.D., 1981. Stable analytical inversion solution for processing lidar returns. Appl. Opt. 20, 211–220.

Klett, J.D., 1985. Lidar inversion with variable backscatter/extinction ratios. Appl. Opt. 24 (11), 1638–1643.

Kirchstetter, Thomas W., Novakov, T., Hobbs, Peter V., 2004. Evidence that the spectral dependence of light absorption by aerosols is affected by organic carbon. J. Geophys. Res. Atmos. 109 (D21) n/a-n/a.

Li, Zhanqing, Chen, H., Cribb, M., Dickerson, R., Holben, B., Li, C., Lu, D., Luo, Y., Maring, H., Shi, G., Tsay, S.-C., Wang, P., Wang, Y., Xia, X., Zheng, Y., Yuan, T., Zhao, F., 2007. Preface to special section on east Asian studies of tropospheric aerosols: an international regional experiment (EAST-AIRE). J. Geophys. Res. 112 (D22).

Lohmann, U., Quaas, J., Kinne, S., Feichter, J., 2007. Different approaches for constraining global climate models of the anthropogenic indirect aerosol effect. Bull. Am. Meteorol. Soc. 88 (2), 243–249.

Mahowald, N.M., Kloster, S., Engelstaedter, S., Moore, J.K., Mukhopadhyay, S., McConnell, J.R., Albani, S., Doney, S.C., Bhattacharya, A., Curran, M.A.J., Flanner, M.G., Hoffman, F.M., Lawrence, D.M., Lindsay, K., Mayewski, P.A., Neff, J., Rothenberg, D., Thomas, E., Thornton, P.E., Zender, C.S., 2010. Observed 20th century desert dust variability: impact on climate and biogeochemistry. Atmos. Chem. Phys. 10, 10875–10893.

Mao, F., Gong, W., Zhu, Z., 2011. Simple multiscale algorithm for layer detection with lidar. Appl. Opt. 50 (36), 6591–6598.

Mikami, M., Shi, G.Y., Uno, I., Yabuki, S., Iwasaka, Y., Yasui, M., Aoki, T., Tanaka, T.Y., Kurosaki, Y., Masuda, K., Uchiyama, A., Matsuki, A., Sakai, T., Takemi, T., Nakawo, M., Seino, N., Ishizuka, M., Satake, S., Fujita, K., Hara, Y., Kai, K., Kanayama, S., Hayashi, M., Du, M., Kanai, Y., Yamada, Y., Zhang, X.Y., Shen, Z., Zhou, H., Abe, O., Nagai, T., Tsutsumi, Y., Chiba, M., Suzuki, J., 2006. Aeolian dust experiment on climate impact: an overview of Japan–China joint project ADEC. Glob. Planet. Change 52 (1–4), 142–172.

Moosmüller, H., Chakrabarty, R.K., Arnott, W.P., 2009. Aerosol light absorption and its measurement: a review. J. Quant. Spectrosc. Radiat. Transf. 110 (11), 844–878.

Nousiainen, Timo, 2009. Optical modeling of mineral dust particles: a review. J. Quant. Spectrosc. Radiat. Transf. 110 (14–16), 1261–1279.

Papayannis, A., Amiridis, V., Mona, L., Tsaknakis, G., Balis, D., Bösenberg, J., Chaikovski, A., De Tomasi, F., Grigorov, I., Mattis, I., Mitev, V., Müller, D., Nickovic, S., Pérez, C., Pietruczuk, A., Pisani, G., Ravetta, F., Rizi, V., Sicard, M., Trickl, T., Wiegner, M., Gerding, M., Mamouri, R.E., D'Amico, G., Pappalardo, G., 2008. Systematic lidar observations of Saharan dust over Europe in the frame of EARLINET (2000–2002). J. Geophys. Res. 113 (D10).

Pappalardo, G., Amodeo, A., Apituley, A., Comeron, A., Freudenthaler, V., Linné, H., Ansmann, A., Bösenberg, J., D'Amico, G., Mattis, I., Mona, L., Wandinger, U., Amiridis, V., Alados-Arboledas, L., Nicolae, D., Wiegner, M., 2014. EARLINET: towards an advanced sustainable European aerosol lidar network. Atmos. Meas.

Tech. 7, 2389—2409.

Ramanathan, V., Crutzen, P.J., Kiehl, J.T., Rosenfeld, D., 2001. Aerosols, climate, and the hydrological cycle. Sci. (New York, N.Y.) 294 (5549), 2119—2124.

Rosenfeld, Daniel, Andreae, Meinrat O., Asmi, Ari, Chin, Mian, de Leeuw, Gerrit, Donovan, David P., Kahn, Ralph, Kinne, Stefan, Kivekäs, Niku, Kulmala, Markku, Lau, William, Schmidt, K. Sebastian, Suni, Tanja, Wagner, Thomas, Wild, Martin, Quaas, Johannes, 2014. Global observations of aerosol-cloud-precipitation-climate interactions. Rev. Geophys. 52 (4), 750—808.

Russell, P.B., Bergstrom, R.W., Shinozka, Y., Clarke, A.D., Decarlo, P.F., Jimenez, J.L., Livingston, J.M., Redemann, J., Holben, B., Dubovic, O., Strawa, A., 2009. Absorption Ångström exponent in AERONET and related data as an indicator of aerosol composition. Atmos. Chem. Phys. Discuss. 9, 21785—21817.

Sasano, Y., 1996. Tropospheric aerosol extinction coefficient profiles derived from scanning lidar measurements over Tsukuba, Japan, from 1990 to 1993. Appl. Opt. 35, 4941—4952.

Sicard, M., Molero, F., Guerrero-Rascado, J.L., Pedros, R., Exposito, F.J., Cordoba-Jabonero, C., Bolarin, J.M., Comeron, A., Rocadenbosch, F., Pujadas, M., Alados-Arboledas, L., Martinez-Lozano, J.A., Diaz, J.P., Gil, M., Requena, A., Navas-Guzman, F., Moreno, J.M., 2009. Aerosol lidar intercomparison in the framework of SPALINET—the Spanish lidar network: methodology and results. IEEE Trans. Geosci. Remote Sens. 47 (10), 3547—3559.

Stier, P., Seinfeld, J.H., Kinne, S., Boucher, O., 2007. Aerosol absorption and radiative forcing. Atmos. Chem. Phys. 7, 5237—5261.

Stith, J.L., Ramanathan, V., Cooper, W.A., Roberts, G.C., DeMott, P.J., Carmichael, G., Hatch, C.D., Adhikary, B., Twohy, C.H., Rogers, D.C., Baumgardner, D., Prenni, A.J., Campos, T., Gao, RuShan, Anderson, J., Feng, Y., 2009. An overview of aircraft observations from the Pacific Dust Experiment campaign. J. Geophys. Res. 114 (D5).

Tanré, D., Haywood, J., Pelon, J., Léon, J.F., Chatenet, B., Formenti, P., Francis, P., Goloub, P., Highwood, E.J., Myhre, G., 2003. Measurement and modeling of the Saharan dust radiative impact: overview of the Saharan Dust Experiment (SHADE). J. Geophys. Res. 108 (D18).

Tian, Pengfei, Cao, Xianjie, Zhang, Lei, Wang, Hongbin, Shi, Jinsen, Huang, Zhongwei, Zhou, Tian, Liu, Hui, 2015. Observation and simulation study of atmospheric aerosol nonsphericity over the Loess Plateau in northwest China. Atmos. Environ. 117, 212—219.

Tian, Pengfei, Cao, Xianjie, Zhang, Lei, Sun, Naixiu, Sun, Lu, Logan, Timothy, Shi, Jinsen, Wang, Yuan, Ji, Yuemeng, Lin, Yun, Huang, Zhongwei, Zhou, Tian, Shi, Yingying, Zhang, Renyi, 2017. Aerosol vertical distribution and optical properties over China from long-term satellite and ground-based remote sensing. Atmos. Chem. Phys. 17 (4), 2509—2523.

Twomey, S., 1991. Aerosols, clouds and radiation. Atmos. Environ. Part A. General Top. 25 (11), 2435—2442.

Wang, X., Huang, J., Ji, M., Higuchi, K., 2008. Variability of East Asia dust events and their long-term trend. Atmos. Environ. 42, 3156—3165.

Wang, Z., Zhang, L., Cao, X., Huang, J., Zhang, W., 2012. Analysis of dust aerosol by using dual-wavelength lidar. Aerosol Air. Qual. Res. 12, 608—614.

Welton, E.J., Campbell, J.R., Spinhirne, J.D., Scott, V.S., 2001. Global monitoring of clouds and aerosols using a network of micro-pulse lidar systems. In: Singh, U.N., Itabe, T., Sugimoto, N. (Eds.), Lidar Remote Sensing for Industry and Environmental Monitoring. SPIE, Bellingham, Wash, pp. 151—158.

Wu, Y., Fan, L., Lin, Y., Zhao, R., Lv, Z., Zhou, J., Han, Y., Yang, M., Ai, W., Zhang, P., Li, Y., Liu, Q., Liao, M., Li, X., Chen, D., Shu, W., 2010. In: Qu, X., Zhang, Y., Zong, Z., Zhang, J. (Eds.), Sand-dust Weather Almanac. China Meteorological Press, Beijing, China, pp. 45—48 (in chinese).

Zhang, K., Gao, H., 2007. The characteristics of Asian-dust storms during 2000-2002: from the source to the sea. Atmos. Environ. 41, 9136—9145.

Zhang, L., Cao, X., Bao, J., Zhou, B., Huang, J., Shi, J., Bi, J., 2010. A case study of dust aerosol radiative properties over Lanzhou, China. Atmos. Chem. Phys. 10, 4283—4293.

Zhang, L., Zhang, L., Zhang, D.L., Zhao, S.Q., Huang, J.P., Zhang, W., Shi, J.S., 2011. Property of black carbon concentration over outskirts of Lanzhou, Northwest China. China Environ. Sci. 31, 1248—1255 (in Chinese).

Zhou, B., Zhang, L., Cao, X., Li, X., Huang, J., Shi, J., Bi, J., 2012. Analysis of the vertical structure and size distribution of dust aerosols over the semi-arid region of the Loess Plateau in China. Atmos. Chem. Phys. Discuss. 12 (2), 6113—6143.

Zhu, Aihua, Ramanathan, V., Li, Fang, Kim, Dohyeong, 2007. Dust plumes over the Pacific, Indian, and Atlantic oceans: climatology and radiative impact. J. Geophys. Res. 112 (D16).